I.M. Viola, P. Bot, M. Riotte

Upwind Sail Aerodynamics: a RANS numerical investigation validated with wind tunnel pressure measurements

International Journal of Heat and Fluid Flow 39 (2013) 90–101
http://dx.doi.org/10.1016/j.ijheatfluidflow.2012.10.004

Keywords: sail aerodynamics, CFD, RANS, yacht, laminar separation bubble, viscous drag.

Abstract

The aerodynamics of a sailing yacht with different sail trims are presented, derived from simulations performed using Computational Fluid Dynamics. A Reynolds-averaged Navier-Stokes approach was used to model sixteen sail trims first tested in a wind tunnel, where the pressure distributions on the sails were measured. An original approach was employed by using two successive simulations: the first one on a large domain to model the blockage due to the wind tunnel walls and the sails model, and a second one on a smaller domain to model the flow around the sails model. A verification and validation of the computed aerodynamic forces and pressure distributions was performed. The computed pressure distribution is shown to agree well with the measured pressures. The sail surface pressure was correlated with the increase of turbulent viscosity in the laminar separation bubble, the flow reattachment and the trailing edge separation. The drive force distribution on both sails showed that the fore part of the genoa (fore sail) provides the majority of the drive force and that the effect of the aft sail is mostly to produce an upwash effect on the genoa. An aerodynamic model based on potential flow theory and a viscous correction is proposed. This model, with one free parameter to be determined, is shown to fit the results better than the usual form drag and induced drag only, even if no friction drag is explicitly considered.

1. Introduction

Research on sailing yacht aerodynamics has grown drastically in the last few years as the competitiveness of sailing races has increased together with improved test methodologies. An understanding of the air flow around the mast and sails is of paramount importance to determine the performance of a sailboat and hence to optimise the sail design and setup during racing. Computational Fluid Dynamics (CFD) is now widely used in sail design. The early works of Milgram (1968a, 1968b), Gentry (1971, 1988) and others were based on potential flow models and enabled great improvements in the understanding of sail aerodynamics. In the last decades, thanks to the large increase of computational capabilities, Reynolds Averaged Navier-Stokes (RANS) solvers have been used, allowing the visualisation of separated flow around sails (for example, Hedges et al., 1996; Miyata and Lee, 1999). When the wind comes from the aft part of the yacht, namely sailing downwind, highly cambered sails are used at a high angle of attack and then the flow is massively separated on the suction side of the sails. Hence, a potential flow model is not relevant and the higher computational effort of a viscous model is necessary. When the wind comes from the fore part of the yacht, namely sailing upwind, slightly cambered sails are used at relatively small angles of attack. For these scenarios the boundary layer can usually be considered to remain attached and potential codes are thus appropriate. However, although non-viscous models may give acceptable estimations of the global aerodynamic forces, results are poor where the viscosity plays a significant role, for example in separated flow areas such as sails tips.

Even though many models are now available for sail aerodynamics, there is a real need for detailed validation of numerical simulations in order to provide reliable design tools for the sailing industry. Unfortunately, realistic and reliable experimental data is scarce and the validation of models in real conditions is difficult. Between the few existing examples, interested readers may consider, for instance, Lasher and Richards (2007) for downwind sail, and Viola et al. (2011) for upwind sails. In those papers the geometries of the sails and the experimental forces or pressure distributions measured in the wind tunnel are provided.

In spite of much recent progress, the physics of the flow around sails is still far from being completely understood. Yacht sails are high-lift thin aerofoils with sharp leading edges. Indeed, sails aerodynamics present many flow features which are difficult to model and are still subject to much research efforts, such as laminar separation, laminar-to-turbulent transition, trailing edge separation in high lift condition and massively separated flow for tight trims. In real sailing conditions, analysis is made more difficult because of the non-homogeneity and unsteadiness of the incoming wind and the yacht motion. Moreover, the fluid structure interaction is strong and highly non-linear because the sails are light membranes subject to large displacements and accelerations. The most recent investigations on the fluid structure interactions of sails are the works of Chapin et al. (2011), Renzsh and Graf (2010), and Augier et al. (2012).

Therefore, more detailed investigations within a controlled environment are necessary to provide new insights into these complex flow features. Common practice in wind tunnel tests is to use flexible model sails, which may be trimmed equivalent to the full scale counterparts. The experiments measure the global aerodynamic forces on the sails and the yacht model together by means of a balance attached to the model. Conversely, when experiments are used to validate numerical simulations, the use of rigid sails allows the geometry to be more precisely defined and reproduced in the numerical model. Pressure measurements over the sail surface enable the analyst to perform a more accurate validation compared to experiments which only measure global forces. Moreover, investigation of the pressure distributions on the sails allows a finer description of the flow behaviour, and thus gives a better understanding of the flow physics.

The contribution of this paper is that RANS simulations on upwind sails are, for the first time, validated with local pressure measurements on fully three-dimensional model-scale sails. In previous works, validation was performed with global quantities such as the aerodynamic forces on the sails (Lasher and Richards, 2007; Viola, 2009), or on a bi-dimensional sail section (Caponnetto and Castelli, 1998, using the data from Wilkinson, 1984). The aim of this work is to develop a reliable RANS simulation on upwind sails with a thorough validation with experimental data and to gain new insights on the flow field correlated with the measured surface pressure distributions. The present work is part of a wide reaching project headed by the first author, investigating sail aerodynamics through full-scale on-water experiments, model-scale wind-tunnel tests and CFD analysis for upwind and downwind conditions (Viola and Flay, 2011a).

The paper is organised as follows. The experimental benchmark used for the simulation validation is briefly described in Section 2. Section 3 presents the numerical arrangements and results are given and discussed in Section 4. The final section is devoted to concluding remarks.

2. Experimental Benchmark

Sails of a candidate America's Cup (AC) class, AC33, were designed and tested in the wind tunnel of the Yacht Research Unit, University of Auckland, for the AC challenger Emirates Team New Zealand. The wind tunnel is an open jet test section, 7 m wide and 3.5 m high. A genoa and a mainsail, which are the sails forward and aft respectively, were designed to 1/15th model scale and were rigidly constructed using fibreglass and a sandwich structure. Pressure taps are holes in the sail surface that connect the sail surface with the core tube inside the sail. Four horizontal rows of holes were drilled on both sails. Further details on the sail construction can be found in Fluck et al. (2010).

Two different experimental setups were tested. In a first experiment (Viola and Flay, 2011b), the sails were fixed to a model scale rigging and hull placed on the floor of the wind tunnel. Aerodynamic forces were measured by a six-component balance located below the wind tunnel floor, and the trim which produced the maximum thrust force was detected. The model heading was 19° from the wind tunnel longitudinal axis. A second experiment was performed with a specific focus on providing a benchmark for numerical methods and thus the experimental setup was simplified (Viola et al., 2011). Fig. 1 shows a schematic drawing of the experimental setup. The sails were suspended with transparent fishing lines in the middle of the wind tunnel test section, i.e. outside the wind tunnel boundary layer. The rigging and the yacht hull were not included. Instead, a wooden square flat plate was placed below the sails to model the non-slip condition due to the water plane and the yacht hull. The plane was at the level of the genoa foot, meaning there was no gap between the genoa and the plane. Additional to the optimum trim measured in the previous experiment, three different genoa trims (namely G1-4 from tight to loose) and three different mainsail trims (namely M1-4 from thight to loose) were tested, producing a total of 16 configurations. The optimum trim is named G3M2. The geometry of the sails can be downloaded from the website ignazioviola.com. The effective sail area of the two sail configuration was $SA = 1.8\ \mathrm{m}^2$, while the reference height computed from the top of the mainsail to the foot of the genoa was $h = 2.3$ m. The reference dynamic pressure q_∞ and static pressure p_∞ were measured at the same height as the top of the mainsail and $6h$ upstream the model. The tests of both experimental setups were performed in uniform wind condition with a dynamic pressure of $q_\infty = 32.5 \pm 1$ Pa and a free stream turbulence intensity of 3%. The Reynolds number, based on the averaged chord of one sail $c = SA/2h$ =0.40 m, was $Re = 2.0{\times}10^5$.

The uncertainty on the position of the sail was estimated to ± 1 mm through repeated measurements along the fishing line. The pressure measurements were also repeated for several configurations after having re-trimmed the sails. The standard deviation of the measured pressure coefficients, defined as $Cp = (p - p_\infty)/q_\infty$, showed that Cp was measured with an uncertainty of ± 0.23 on the suction side and ± 0.08 on the pressure side with a confidence level of 95%.

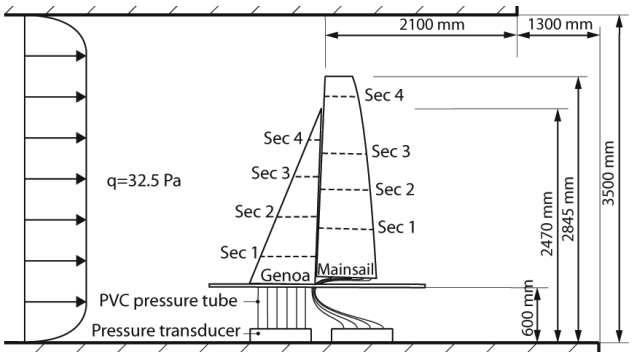

Fig. 1. Experimental setup (edited from Viola et al., 2011).

3. Numerical Model

The wind tunnel experiments on the 16 sail configurations were modelled with RANS simulations. Hexahedral grids were built with the commercial software Ansys ICEM CFD, version 12.0.1, which is a top-down approach mesher renowned for its high quality features to make hexahedral grids, while the finite volume commercial software Ansys Fluent, version 12.0.1, was used to solve the RANS equations. In particular, the steady pressure based solver was used to solve the incompressible Navier-Stokes equations for Newtonian fluids. Two different two-equation turbulence models were used. A SIMPLEC scheme was used to couple velocity and pressure. Second order accuracy discretization algorithms were used because third order accuracy algorithms showed difficulty to converge. Simulations were performed with an Intel Core i5 processor 3.2 GHz, 3GB of RAM and Windows XP Professional operating system.

The convergence of the simulations was verified by monitoring the lift and drag of the sails together with the maximum and minimum pressures along the lowest measurement sections of each sail. Convergence was achieved when each of these monitored values and the residuals showed oscillations around a constant mean value of the order of 10^{-3} or less. Most of the simulations required a total *wall-clock time* (CPU time, I/O time, and communication channel delay) of about 12 hours.

Sails are thin aerofoils with a sharp leading edge, thus even a very slight variation of the angle of attack may have a significant effect on the flow field. In particular, when the streamline just upstream the sail is parallel to the surface near the leading edge, there is no leading edge separation on either side of the sail. A yacht in upwind condition often sails in this condition (Viola and Flay, 2010), known as the *ideal angle of attack*. At any angle higher or lower than the ideal, the stagnation point is either on the pressure or the suction side respectively. The flow separation occurs on the side opposite to the stagnation point (Viola and Flay, 2011b). For this reason, special care must be devoted to precisely compute the incoming flow field taking into account the blockage effect of the wind tunnel walls.

It is known that the accuracy of numerical simulations performed with RANS approach generally improves with a higher grid resolution. However, a higher grid resolution results in an increased computational time and also requires more RAM to solve the system of equations. Therefore, in practice, the maximum accuracy of the simulation depends on the computational resources available. In the present paper, in order to model with good grid resolution different features of interest, two models were investigated. The first model, described in Section 3.1, focused on investigating the blockage effect due to the wind tunnel

walls and the sails model. In this model, the boundary layer on the wind tunnel walls was solved with high grid resolution, while the sails' boundary layer was neglected using a slip condition. The velocity field on the wind tunnel jet section, computed from the blockage model, was imported into a second model, detailed in Section 3.2. In this the wind tunnel walls were not modelled, while the sails' boundary layer was solved with high grid resolution. This method allows all the computational resources available to be focused on one feature at a time: the boundary layer on the wind tunnel walls in the first model and on the sails in the second model. Therefore, the accuracy in the computation of each feature is enhanced compared with a single model approach, where the computational resources are split to solve at the same time the boundary layers on the wind tunnel walls and on the sails. Moreover, and important to note, two different turbulence models have been used in the models to better suit the flow features in each case (see Sections 3.1 and 3.2).

3.1. Blockage Model

The first model was aimed at investigating the blockage effect and thus the combined effect on the flow field due to the wind tunnel side walls and roof, and the yacht sails model. A cuboid domain $12h$ wide, $12h$ long and $1.3h$ high was modelled. Fig. 2a shows a schematic drawing of the domain and shows the boundary conditions used on each face of the domain. The bottom face of the cuboid represents a horizontal section of the wind tunnel at 600mm height from the floor, which is the same height as the horizontal plate shown in Fig. 1. Therefore, the simulation does not model the wind-tunnel floor boundary layer. The upper face of the cuboid represents a horizontal section of the wind tunnel at its roof height. It should be noted that, as shown in Fig. 2, the wind tunnel roof extends $2.5h$ downstream the jet section. The sidewalls of the wind tunnel are modelled with zero thickness surfaces and $3.1h$ offset, which corresponds to the jet section width.

The aim of this model is to compute the velocity field on the jet section, which is then used as the inlet condition in the second model (Section 3.2). The model was thus designed to compute with high accuracy the streamline deflection due to the lift generated by the sails and affected by the presence of the wind tunnel walls. This was achieved by using a high grid resolution for the boundary layer on the sidewalls and on the roof, while the boundary layer on the sails is neglected using a slip condition. In this model, only the sail configuration corresponding to the trim allowing the maximum drive force is considered.

A grid of about one million cells was performed allowing $y+< 5$ on the tunnel walls. The $k-\varepsilon$ *realizable* turbulence model was used, which is renowned for its robustness and accuracy in attached flow condition (Shih et al., 1995). An inlet uniform flow speed with 3% turbulence intensity and turbulent viscosity ten times the fluid viscosity was used.

3.2. Sails Model

The velocity field computed on the jet section was imported into the second model, which aimed to investigate the flow field around the sails. Therefore, a shorter domain was used, where the inlet face of the domain was located in correspondence to the jet section. High grid resolution was used to solve the boundary layer on the sail surfaces. Fig. 2b shows a schematic drawing of the model and shows the boundary conditions adopted. Fig. 3 shows a horizontal layer and a transversal layer of the grid near the sails. The grid comprised about 1.4 million hexahedral cells. Sail surface cells had different surface-normal dimensions on both sides of the sails. On the suction (leeward) side, where regions with separated flow occur,

$y+ < 3$ was used. On the pressure (windward) side, where the boundary layer is always attached, $5 < y+ < 25$ was used. The $k - \omega$ SST turbulence model was employed because of its ability to model strong adverse pressure gradients and separation in the aeronautical field (Menter, 1993). It is known for its superior performance in the near wall region compared to $k - \varepsilon$ models (Menter et al., 2003).

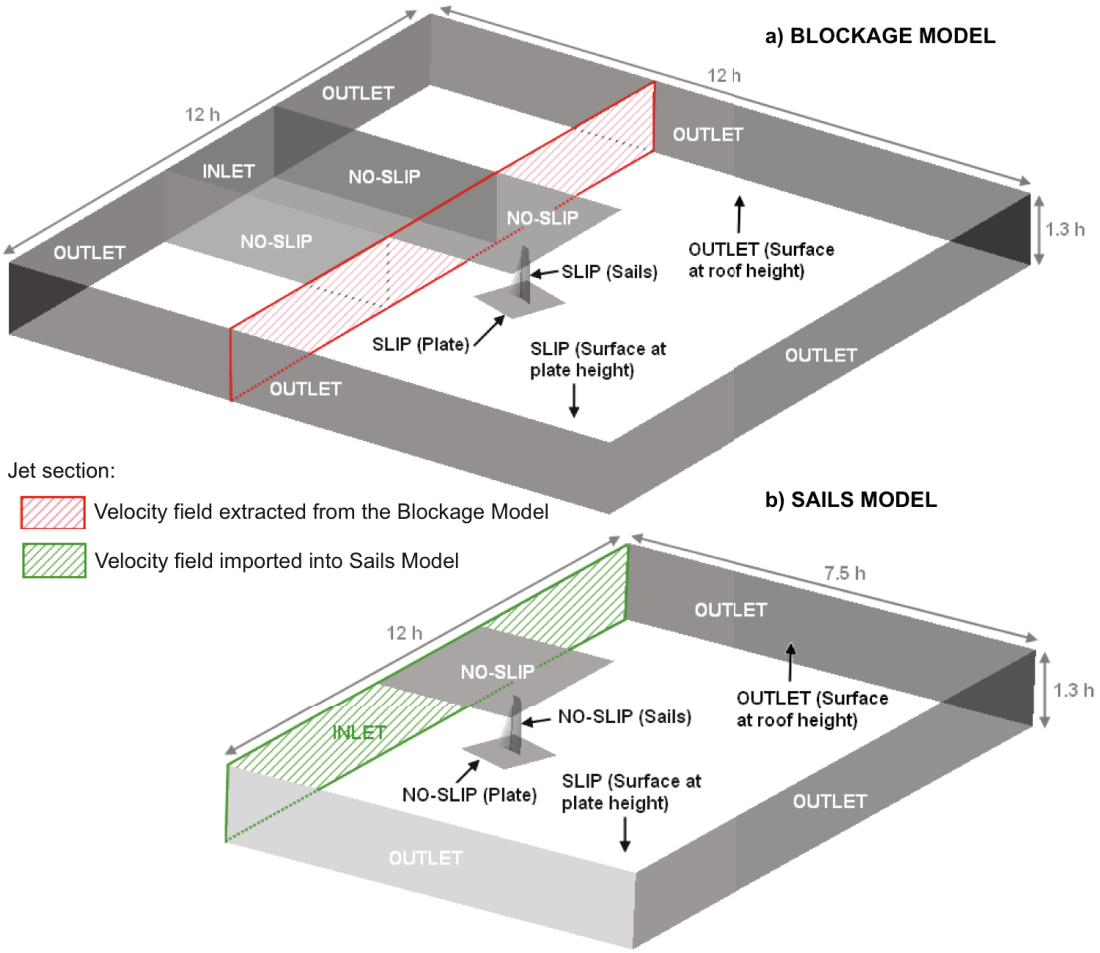

Fig. 2. Domain size and boundary conditions used to compute the flow field at the jet section (a. Blockage Model) and to compute the flow field around the sails (b. Sails Model).

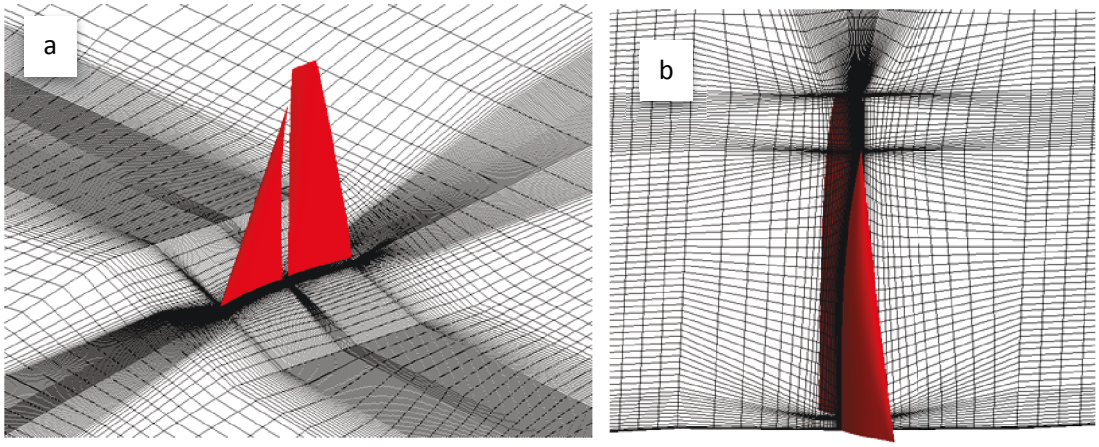

Fig. 3. A horizontal (a) and a transversal (b) layer of the grid near the sails.

3.3. Verification and Validation

Computed pressures were compared with the experimental data for all 16 tested trims and good agreement was found for all cases. For instance, Fig. 4 shows the computed and measured *Cp* along the chord-wise x axis for the four sections of the two sails for the optimum trim (G3M2).

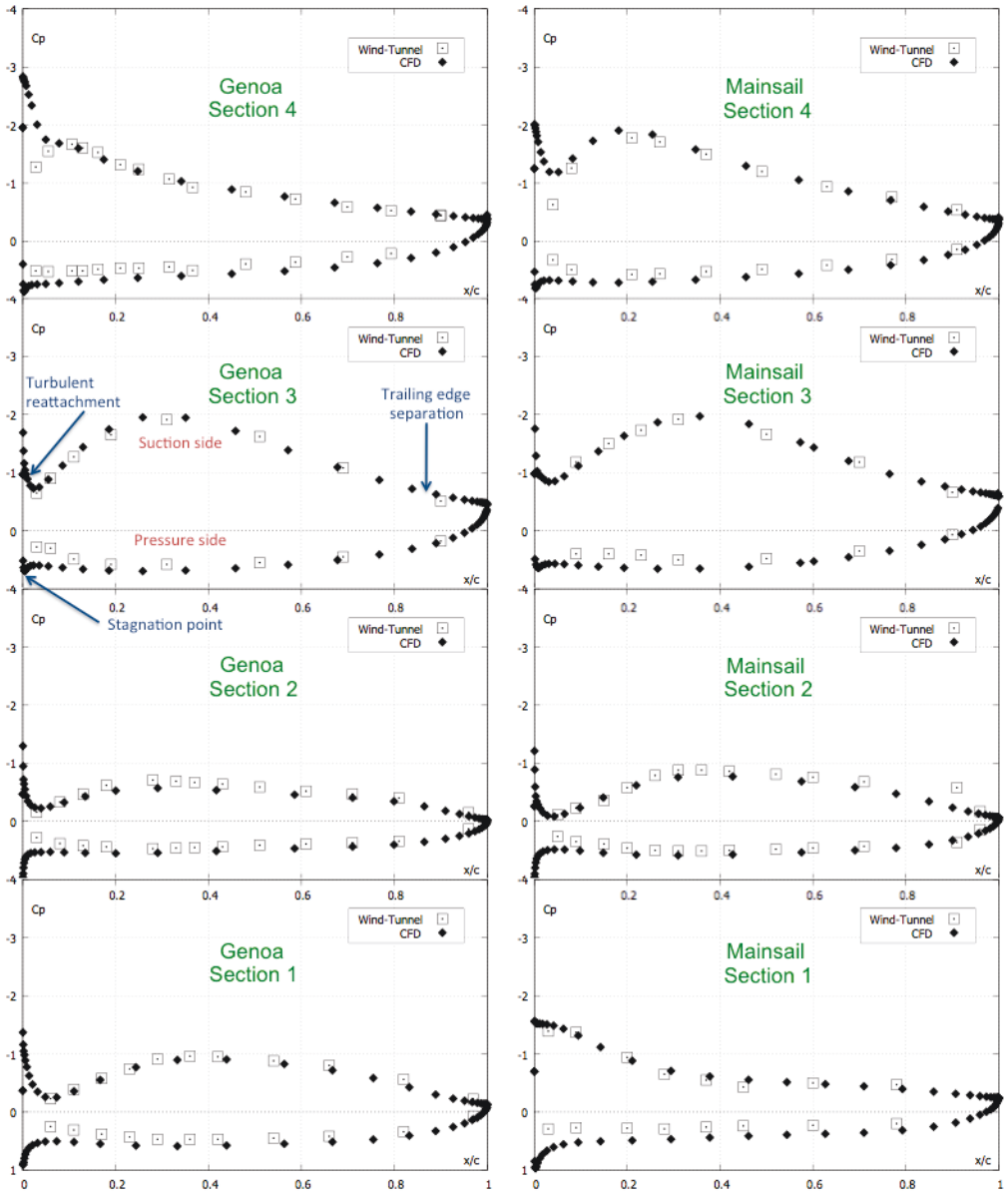

Fig. 4. *Cp* on Sections from 1 (top) to 4 (bottom) of the genoa (left) and mainsail (right) for the optimum sail trim (G3M2).

Similar agreement was found for the other trims. As an example, Fig. 5 and 6 show the computed and measured *Cp* along the sail sections that experienced the minimum and the maximum flow separation, which are Section 2 of the genoa for the loosest trim (i.e. lowest angle of attack) and Section 4 of the mainsail for the tightest trim (i.e. highest angle of attack), respectively. When the flow is fully separated (Fig. 6), *Cp* is computed with high accuracy for both the pressure and suction side of the sail. When the flow is attached, *Cp* is computed with high accuracy on most of the sail section but the agreement is lower near the leading edge. In

fact, when the flow that separates at the leading edge reattaches downstream along the sail section, the pressure at the leading edge is very sensitive to small differences in the angle of attack, which leads to large numerical and experimental uncertainties. For instance, Fig. 5 shows poor agreement near the leading edge for both the pressure and suction sides. On the suction side, this can be due to an incorrectly computed deflection of the streamlines upstream of the leading edge, or to an incorrect measurement of the leading edge angle of the sail section. On the pressure side, this can be due to a modelling error. In fact, the numerical model had zero thickness while the experimental model had a thickness of about 1% of the sail chord, and the sails were chamfered at about 20° on the windward side to produce a sharp leading edge. Therefore, on the experimental model, the closest pressure taps to the leading edge on the windward side are downstream from a sharp angle, which leads to an acceleration of the flow and a drop in pressure.

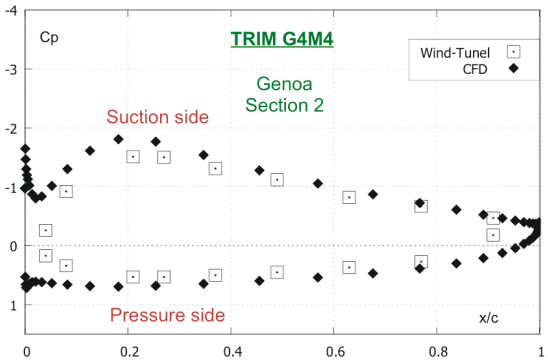

Fig. 5. *Cp* on Section 2 of the genoa for the loosest mainsail and genoa trim (G4M4), which corresponds to the minimum flow separation.

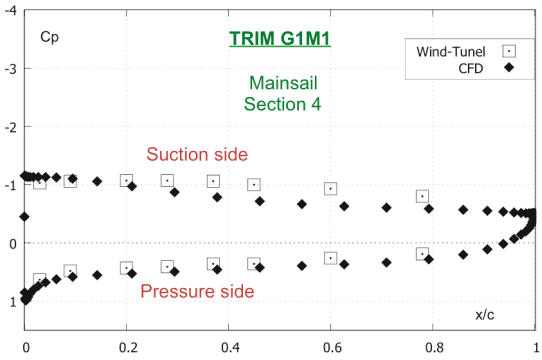

Fig. 6. *Cp* on Section 4 of the mainsail for the tightest mainsail and genoa trim (G1M1), which corresponds to the maximum flow separation.

The analysis of the aerodynamic forces showed that trim G3M2 allowed the maximum drive force, in agreement with the experimental results.

Verification and validation (V&V) was performed with the aim of assessing numerical and model uncertainty on the lines suggested by Eça et al. (2010). In particular, uncertainties were estimated for the global lift and drag allowed by the two sails together, and for the pressure measured on four sail sections of each sail. Pressures were also validated with the experimental measurements.

The convergence uncertainty was taken as the difference between the last computed value and the asymptotic value, which was computed with the least-squares method. In addition, this difference was multiplied by a factor of safety $F_s = 1.25$. The simulations were stopped when the convergence uncertainties for all monitored quantities were lower than 0.1% over the last 1000 iterations. The round-off uncertainty was taken as the difference between the values computed with single and double precision on a 64-bit machine, multiplied by $F_s = 3$. For every monitored quantity, this result was lower than 0.1%.

The discretisation uncertainty was assessed with five grids with relative step ratio (ratio between the mean node distances of each grid and the base grid) $h = 2^{-\frac{1}{3}}$, 1 (base grid), $2^{\frac{1}{3}}$, $2^{\frac{2}{3}}$, and 2. The lift did not show a converging trend with h. Therefore, the uncertainty was taken as the L_∞ norm (maximum difference between computed values defined as

$\|C_L\|_{L_\infty} = \max(C_{L_i}) - \min(C_{L_i})$ multiplied by $F_s = 3$. This resulted in a discretisation uncertainty for the lift of 0.9%. The drag showed a convergence trend and, thus, a least-squares fit was used to compute the extrapolated drag for $h = 0$. The fit error was negligible and the uncertainty was taken as the difference between the computed and extrapolated drag, multiplied by $F_s = 1.25$. For the reference grid, this resulted in a discretisation uncertainty for the drag of 1.5%.

The L_2 norms (Euclidean distances defined as $\|C_p\|_{L_2} = \sqrt{\sum_i {C_p}_i^{\,2}}$) of the pressure coefficients computed for each of the four sections of the two sails (Fig. 1) were computed and their uncertainties were assessed. These showed converging trends with negligible fit errors and $F_s = 1.25$ was used. Table 1 shows the discretisation, experimental and validation uncertainties, and the numerical-experimental differences for the four genoa sections (FS) and the mainsail sections (MS). These differences are smaller than the validation uncertainties, meaning that the simulations are successfully validated.

Table 1. Validation of the L_2 norm of the pressure coefficients

	FS1	FS2	FS3	FS4	MS1	MS2	MS3	MS4
U^{discr}	0.064	0.018	0.007	0.021	0.028	0.064	0.15	0.068
U^{conv}	0.021	0.021	0.021	0.021	0.021	0.021	0.021	0.021
U^{num}	0.085	0.039	0.028	0.042	0.049	0.085	0.171	0.089
U^{exp}	0.681	0.703	0.687	0.660	0.811	0.811	0.764	0.687
U^{val}	0.687	0.704	0.688	0.661	0.812	0.815	0.783	0.693
$\left\|\|C_p\|_{L2}^{num} - \|C_p\|_{L2}^{exp}\right\|$	0.571	0.384	0.169	0.035	0.144	0.227	0.168	0.023
Validation	yes	yes	yes	yes	yes	yes	yes	yes

4. Results and Discussion

The numerical analysis allows a wide range of additional information to be analysed on top of the experimental measurements. For example:

1. Numerical analysis allows higher spatial resolution of the pressure distribution than the experimental setup, particularly near the leading and trailing edges where it is difficult to fit pressure taps;
2. Regions of attached and separated flow can be easily detected and correlated with the pressure distribution;
3. The boundary layer can be investigated with high spatial resolution, particularly in the near wall region where wind measurements can be difficult, and conditions for separation can be identified;
4. Laminar to turbulent transition and turbulent wakes can be identified and characterised by means of statistical quantities, and conditions for reattachment and separation can be identified.

The results presented herein are focussed on the first two points above, while further on-going research is focussed on the third and fourth points, where boundary layer integral quantities are investigated by means of turbulence models designed to model the laminar-to-turbulence transition.

The computed blockage effect is discussed in Section 4.1, where the benefits of the original modelling approach are highlighted. In Section 4.2, the flow field around the sails is discussed and, particularly, the computed velocity field is correlated with the experimentally measured pressure distributions. In Section 4.3, different trims and the correlated flow fields are considered. In particular, the extension of the region with separated flow is correlated with the computed aerodynamic forces for different sail trims, and the most common aerodynamic model based on potential flow theory is modified to take separation into account.

4.1. Blockage Effect

During wind flow experiments in a wind tunnel, a boundary layer grows along the wind tunnel walls, leading to an accelerated flow in the middle of the channel and to slower velocity nearer the walls. The circulation correlated with the lift force on the sails model leads to a deflection, namely upwash, of the streamlines towards the suction side of the sails. As a result, the velocity field at the jet section is non uniform and, on the suction side, the velocity is higher than on the pressure side. Fig. 7 and 8 show the contours on the jet section of the velocity magnitude increase and the upwash angle α, respectively, where α is defined as the horizontal angle between the longitudinal tunnel axis and the velocity vector. The model is shown in transparency in the centre of each figure. The wind speed in front of the model increases from 0.6% to more than 1.2% compared to the uniform inlet velocity. The maximum upwash angle, $\alpha = 0.25°$, occurs in front of the model. The upwash is reduced by the wind tunnel walls, which tend to keep the streamlines straight.

Although this implies the use of different approximations, it can be interesting to compare the computed maximum upwash with the theoretical upwash due to an irrotational vortex centred in the model location and generating the same lift than the sails. With the sail lift coefficient computed in this simulation, $C_L = 1.95$, the circulation Γ is given by $\Gamma = L/(\rho U_\infty b)$, where L is the lift force, ρ is the density, U_∞ is the free stream velocity and b is the equivalent span, which was assumed to be $b = 2h$. The vortex strength is given by $k = \Gamma/2\pi$, and the tangential velocity u_θ at a distance r upstream the model is given by $u_\theta = k/r$, where $r = 1.56h$ is the distance from the model location to the jet section. Finally, the upwash is given by $\alpha = \text{atan}(u_\theta/U_\infty) = 0.6°$. Therefore, the upwash angle computed with the RANS solver taking into account the wind tunnel sidewalls is less than half than the value obtained with potential flow theory for an equivalent isolated vortex.

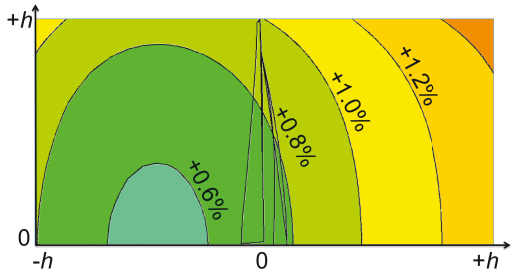

Fig. 7. Contours of the velocity magnitude increase on the jet section.

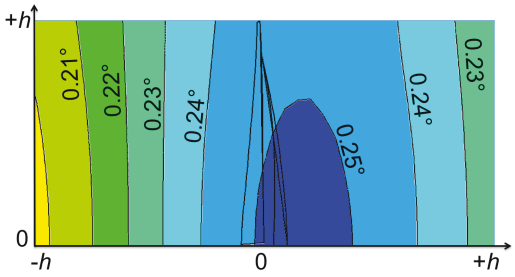

Fig. 8. Contours of the upwash angle α on the jet section.

Fig. 7 and 8 show that the flow at $1.56h$ upstream the model is accelerated and deflected, as a result of the circulation of the sails and the presence of the wind tunnel walls. The presence of the wind tunnel walls tends to increase the aerodynamic forces due to a higher wind speed

and to decrease these forces due to a reduced upwash. It is possible to provide a rough estimation of the effect of the wind speed increase and of the reduced wind deflection on the lift and drag of the sails. In fact, the aerodynamic forces increase with the square of the velocity. Therefore, for instance, a 0.8% increase in wind speed leads to a 0.64% increase in dynamic forces and, thus, in the aerodynamic coefficients defined with the unperturbed reference dynamic pressure q_∞. The upwash reduction leads to a reduction of the aerodynamic forces that can be estimated by considering the correlation between the aerodynamic forces and the angle of attack of an airfoil in potential flow. Assuming an elliptical planform and irrotational flow, the aerodynamic coefficients of a wing can be computed from the angle of attack and the aspect ratio, AR. The lift and drag coefficient variations, δC_L and δC_D respectively, due to a deflection of the free stream $\delta\alpha$, can be written in a first approximation for small angles (since $sin(\alpha) \approx \alpha$):

$$\delta C_L = \frac{2\pi\ \delta\alpha}{1+\frac{2}{AR}}, \delta C_D = \frac{(\delta C_L)^2}{\pi\ AR}, \text{where } AR = \frac{(2h)^2}{SA} \quad (1)$$

In particular, for an upwash reduction of $\delta\alpha = -0.25°$, the lift and drag coefficient variations are $\delta C_L = -0.023$ and $\delta C_D = -0.000015$, respectively. Given the lift and drag coefficient of the reference trim $C_L = 1.27$ and $C_D = 0.152$, respectively, the lift and drag coefficient variations are $\delta C_L = -1.8\%$ and $\delta C_D = -0.010\%$, respectively. Therefore, assuming a wind speed increase of 0.8% and an upwash reduction of $-0.25°$ due to the wind tunnel walls, the addition of these two effects leads to a net lift decrease and drag increase (Table 2). In fact, the lift and the drag increase equally due to the higher wind speed, while the lift decreases significantly more than the drag due to the upwash reduction. As a very small angle of attack variation may yield a significant flow modification – particularly a separation at the leading edge – the blockage model is particularly helpful to precisely determine the flow hitting the sails.

Table 2. Blockage effect

	δC_L	δC_D
Wind speed increase (0.8%)	+0.64%	+0.64%
Upwash reduction (-0.25%)	-1.80%	-0.01%
Total blockage effect	-1.16%	+0.63%

4.2. General Flow Field

It is common practice to consider the aerodynamic force projection on a plane perpendicular to the yacht mast, assuming that the along-the-mast component is negligible. In the present paper where an upright condition is modelled, the plane perpendicular to the mast is horizontal. The aerodynamic force component in the vertical direction is less than 4% of the aerodynamic force magnitude. The projection of the aerodynamic force F on the horizontal plane is described by the lift and drag components, which are in the cross-stream and stream-wise directions respectively. Alternatively, the drive force and the side force components can be used. Non dimensional coefficients C_L, C_D, C_X, C_Y are used to describe the lift, drag, drive and side forces respectively, where the force components are divided by the reference dynamic pressure q_∞ and the sail area SA. Fig. 9 shows how C_X and C_Y are correlated with C_L and C_D, and the effect of a change in the sail trim. A tighter sail produces a higher angle of attack. Trimming in the sail leads the lift to increase until large trailing edge separation occurs,

then causing the lift to decrease. The trim allowing the maximum C_L/C_D is a looser trim – i.e. lower angle of attack – than that allowing the maximum C_X, which is itself a looser trim than that allowing the maximum C_L. In this section (Section 4.2), results for sail trims allowing the maximum C_X (optimum trim) are discussed, while in the following section (Section 4.3) results for different trims are presented.

In order to optimise the trim at every sail section and to take into account the lift distribution which affects the induced drag, the optimum trim results in a twisted sail shape even in a uniform vertical wind profile, such as in the present experiment. Fig. 10 shows the angle between the chord and the hull centreline at 1/4th, 1/2nd and 3/4th of the height of each sail (twist). Also, for each section, the maximum camber and its chord-wise position (draft) are shown in percentage of the chord length.

The upstream sail (the genoa) experiences the upwash due to the downstream sail (the mainsail), while the downstream sail experiences the downwash due to the upstream sail (Gentry, 1971). As a consequence, the mainsail is trimmed tighter – i.e. with lower angle from the centreline – than the genoa in order to increase its angle from the centreline (Fig. 10). Therefore, most of the drive force is due to the genoa, which is trimmed at lower angles of attack and thus gives a higher forward projection of the aerodynamic force than the mainsail. For the same reason, the aerodynamic force due to the forward part of each sail provides a greater contribution to the drive force than the aerodynamic force due to the aft part. Fig. 11 shows the distribution of the local drive force coefficient C_X, which is computed from Cp and the orientation of the surface of each grid cell. The lightest colour band (from -0.5 to 0) shows the region of the sails that provide a negative drive force. The chord at the foot of the mainsail is almost parallel to the yacht centreline and, therefore, the drive force due to the lowest sections of the mainsail is almost zero, if not negative, while the twist of the highest sections allows a better forward projection of the aerodynamic force. Conversely, the lift generated by the mainsail allows the genoa to experience an upwash, which increases the drive force of the genoa. While the genoa experiences a maximum local drive force coefficient of 2.2, this is only 0.91 on the mainsail. Therefore, when trimming the sails to the optimum combined genoa and mainsail drive force, the mainsail is trimmed tighter and nearer the maximum lift condition than the genoa, leading to a lower contribution to the drive force and a higher upwash on the genoa. The (global) drive force coefficient is the surface integral of the local drive force coefficient on both the suction and pressure sides. In particular, the drive force coefficient of the genoa is 0.475, while it is only 0.127 for the mainsail. Together, the two sails achieve a drive force coefficient of 0.270. Results on the aerodynamic coefficients are given in Section 4.3.

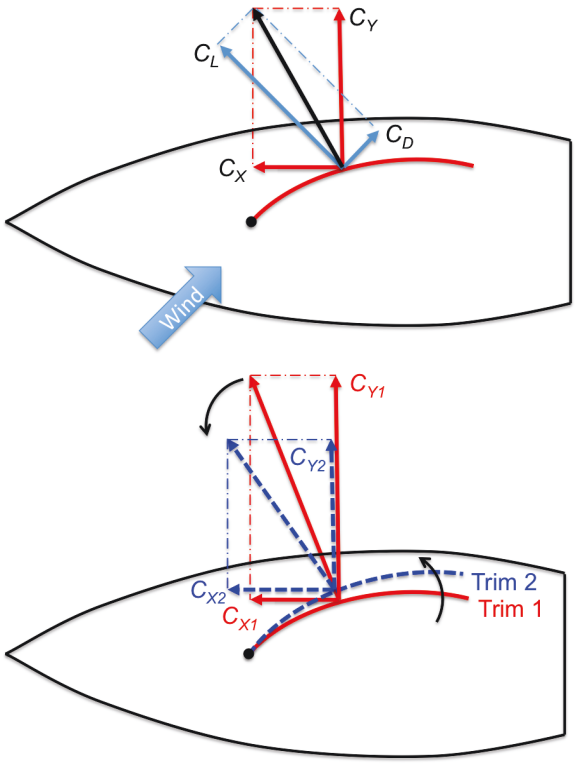

Fig. 9. Breakdown of the aerodynamic force and effect of a trim variation.

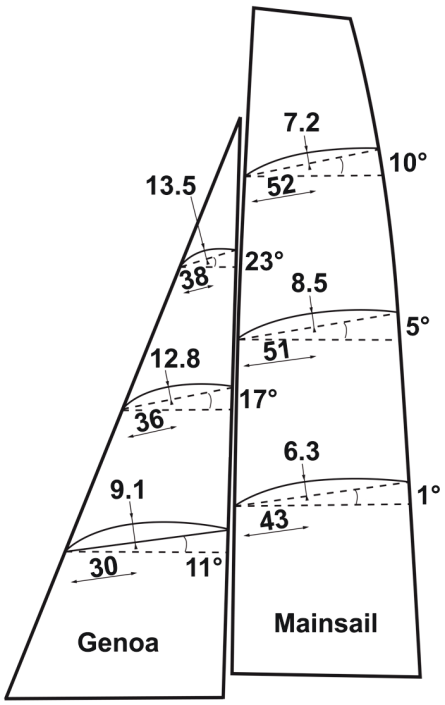

Fig. 10. Draft/chord, maximum camber/chord (in %) and twist angle from the centreline of three sail sections.

The sails are thin airfoils with sharp LE. The stagnation point is on the pressure side of both sails. Downstream from the stagnation point, a laminar boundary layer grows. On the pressure side, the smooth pressure gradient allows the boundary layer to remain laminar for a significant part of the chord. Conversely, on the suction side, the flow separates at the sharp LE. The unstable separated laminar shear layer triggers the transition towards turbulent flow, which thus reattaches forming the so-called laminar separation bubble (LSB). The reattached turbulent boundary layer grows until eventually trailing edge (TE) separation occurs. Fig. 12 shows the attached and separated areas on the suction side of the sails. The LSB occurs along the entire LE of both sails, although the reattachment occurs more downstream on the mainsail and the lower sections of the genoa because of the higher angle of attack. TE separation occurs along most of the TE of both sails and it is more significant on the mid top sections, due to the higher sail curvature in these sections. A significant region of separated flow occurs near the lowest edge of the LE, namely the tack, of both sails. This is due to the small curvature of the lowest sections near the LE. This leads to a high angle between the streamline and the sail section and to a retarded reattachment. Finally, a large region of separated flow occurs on the mainsail downstream the top of the genoa. This is due to the tip vortex of the genoa. On the suction side, about 10% and 20% of the sail area of the genoa and mainsail, respectively, presents a separated flow.

Fig. 13 shows the contours of the turbulent viscosity ratio (turbulent viscosity divided by the physical viscosity of the fluid) on a horizontal plane at the height of the genoa's Section 3 (Fig. 1). The region near the genoa section is shown on the right and a detail of the region

near the LE is shown on the left. The stagnation streaklines are also shown on the suction side of the sail, which is the upper side in the figure. At the LE, the turbulent viscosity increases significantly in the middle of the LSB due to the instability of the laminar shear layer. At about 85% of the chord length, trailing edge separation occurs leading to a significant increase of the turbulent viscosity.

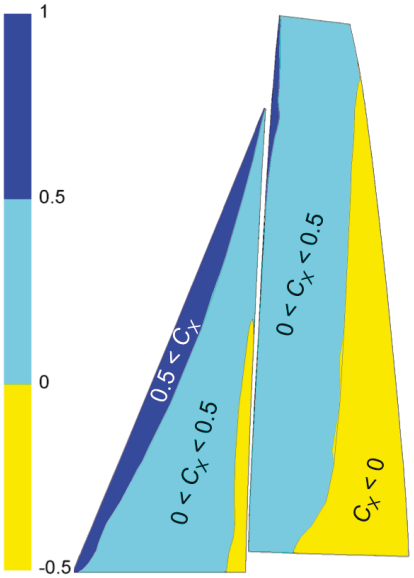

Fig. 11. Distribution of the local drive force coefficient on the suction side of the sails

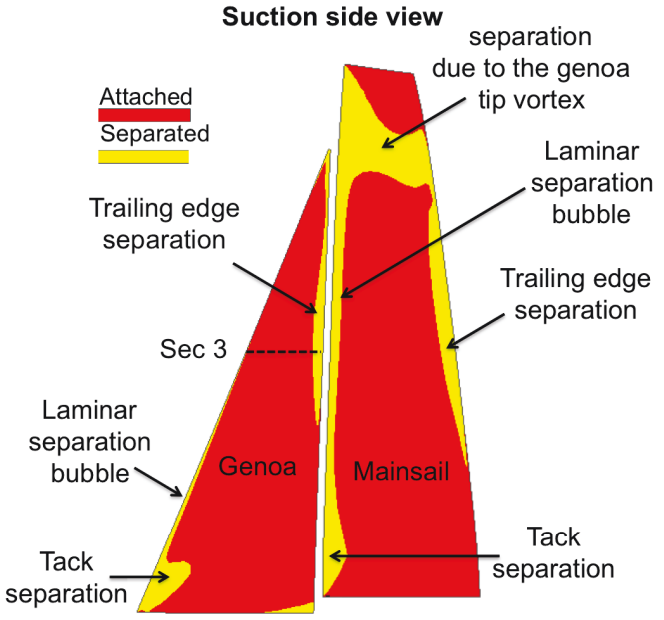

Fig. 12. Separated and attached flow regions on the suction side of the genoa and mainsail

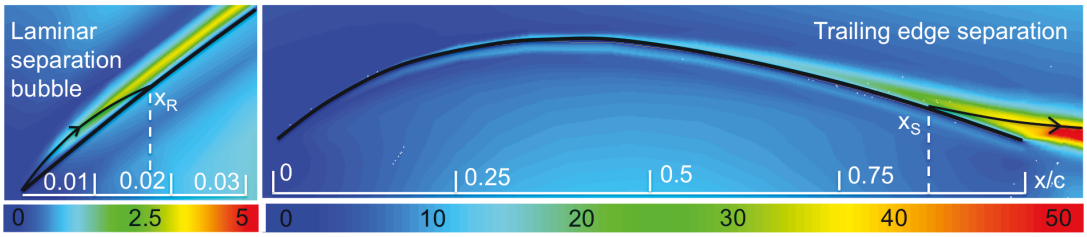

Fig. 13. Contours of turbulent viscosity ratio on the genoa section # 3 (right) and details of the LE region (left).

The pressure distribution correlated with the flow field presented in Fig. 13 is showed in Fig. 4 (Genoa Section 3). On the suction side, two suction peaks occur: the LE suction peak that is correlated with the sharp LE, and a second suction peak around 30% of the chord length that is correlated with the sail curvature. The first suction peak occurs at the second grid cell in the chord-wise direction from the LE. Therefore, the distance of this peak from the LE cannot be accurately determined with the present grid resolution. Downstream of the LE suction peak the maximum adverse pressure gradient occurs, which favours the laminar to turbulent transition on the LSB shear layer. The local maximum pressure is between 2% and 3% of the chord length, which is just downstream of where the reattachment occurs (Fig. 13). Therefore the reattachment occurs in an adverse pressure gradient. It is interesting to note that the local maximum pressure recovery is between the first pressure tap and the LE and, therefore, it was

not possible to measure its location experimentally. The second suction peak is very much smoother than the LE peak. However, the second adverse pressure gradient leads to separation at about 85% of the chord length.

On the pressure side, a maximum pressure correlated with the stagnation point occurs very close to the LE, at less than 1% of the chord length. The stagnation *Cp* on this section is lower than $Cp = 1$ because there is a span-wise velocity component. On the pressure side downstream from the stagnation point, the pressure decreases until about 3% of the chord length, where the pressure starts increasing again due to the sail curvature. Downstream the maximum sail curvature, the pressure decreases with a steeper and steeper gradient until the TE, where it matches the pressure on the suction side.

4.3. Aerodynamic Forces versus Sail Trims

The trim that maximises C_X is not necessarily the same as the trim producing maximum boat speed. In fact, the maximum C_X might be associated with a very large C_Y, which leads to a higher hydrodynamic resistance. In strong breeze conditions, where q_∞ and the forces are large (F_Y in particular), the maximum boat speed is achieved for looser trims where the side force leads to a non-excessive leeway and heel angle. Conversely, in light wind condition, where q_∞ and the forces are small, the side force does not lead to a great resistance penalty and the maximum boat speed is achieved when the sails are trimmed near the maximum C_X.

In the present paper, light wind condition was considered and therefore the sail trims around the optimum trim, maximising F_X, were investigated. Fig. 14 shows the computed C_X versus C_Y for all the 16 configurations. Each curve shows the coefficients computed for one mainsail trim and four genoa trims. Numbered mainsail and genoa trims from one to four are ordered from the tightest to the loosest trim, and therefore from the highest to the lowest angle of attack. Fig. 14 shows that the maximum C_X is achieved for the trim G3M2. When the sails were experimentally tested attached to a model scale rigging and hull (see Section 2) allowing the aerodynamic forces to be measured, the same sail trim was found to allow the maximum C_X. From the optimum trim, when the genoa or the mainsail is tightened, C_Y increases and C_X decreases, while if one of these is loosed, both C_X and C_Y decrease. The trends shown in Fig. 14 are in agreement with the experimental results in the literature (Campbell, 1997; Fossati et al., 2006).

The dotted lines in Fig. 15 show the drag coefficient versus the lift coefficient squared for the 16 trims. As expected from the experimental knowledge (Claughton, 1994; Fossati et al., 2006), the maximum drive force is achieved for a looser sail trim than the trim allowing the maximum lift. In Fig. 15, the maximum lift is achieved by the tightest genoa trim (G1) for most of the mainsail trims (M2-4). Only when the mainsail is already over-trimmed (M1), the maximum lift is achieved for a looser genoa trim (G2). Therefore, the trim allowing the maximum drive force is looser than the trim allowing the maximum lift. Conversely, it is tighter than the trim allowing the maximum lift/drag ratio, which, between the set of tested trims, is the loosest genoa and mainsail trim (M4G4).

When the lift decreases, the gradients of all the four curves tend to converge towards a common value. This gradient is the slope of the dotted line in Fig. 15. Assuming an irrotational flow and elliptic sail planform, the drag coefficient of the sail planform can be expressed as the sum of a lift-independent component, namely the form drag coefficient (C_{D_0}), and a component proportional to the lift squared, namely the induced drag:

$$C_D = C_{D_0} + \frac{{C_L}^2}{\pi\, AR} \tag{2}$$

This irrotational model shows that the drag increases linearly with the squared lift, which is in agreement with the computed results as shown by the dotted line in Fig. 15. The intercept of the dotted line with the ${C_L}^2 = 0$ axis is the form drag C_{D_0}. This drag component is almost negligible. For instance, if C_{D_0} is estimated with Equation (3) (Schlichting and Gersten, 2000), which is valid for turbulent flow on smooth flat plates, then C_{D_0} is about 3% of the total drag coefficient.

$$C_{D_0} = \frac{0.031}{Re^{1/7}} = 0.0046 \tag{3}$$

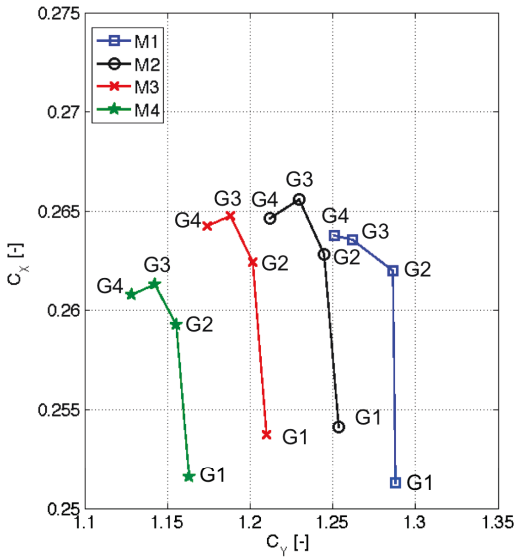

Fig. 14. C_x versus C_y for four mainsail trims (M1-4) and four genoa trims (G1-4).

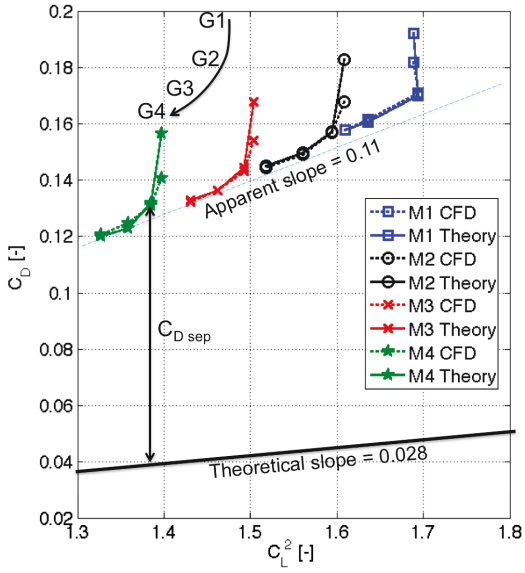

Fig. 15. C_D versus ${C_L}^2$ computed with CFD simulations (dotted line) and with Equation 4 (solid line).

4.4. Limitations of the irrotational model

Fig. 15 shows that the drag increases linearly with the square of the lift only for loose trims, while it increases more than linearly for tight trims. The linear increase can be associated with the induced drag, while excess drag can be associated with flow separation. However, the loosest trims also have regions with separated flow. Fig. 16 shows the attached and separated areas on the suction sides of the genoa and mainsail for four different trims. In particular, the following trims are presented: G1-4M2 and G3M1-4. Therefore, the irrotational model, which does not take into account the drag due to the separation, is unable to predict correctly the slope of the total drag. In fact, the model predicts a theoretical slope of $(\pi\, AR)^{-1} = 0.028$, while the computed apparent slope is 0.11. In addition, the intercept of the apparent slope with the ${C_L}^2 = 0$ axis is a negative value (-0.027), while the irrotational model assumed that the intercept is equal to the form drag, which is positive by definition. The present results show that the theoretical model is inadequate for those trims that are used in light wind, such as the ones presented here.

Fig. 17 shows the differences between the computed drag coefficient and the theoretical drag coefficient computed with Equation (2). This difference, $C_{D_{sep}}$, is assumed to be due to separation and may be considered as a pressure drag coefficient. In particular, for each mainsail trim, the tightest genoa trim that was unrealistically tight and where flow was separated on most of the sail area, was not considered. Fig. 17 shows that $C_{D_{sep}}$ increases linearly with the sail area where the flow is separated with a slope $k = 0.31$. Therefore, $C_{D_{sep}}$ can be added to Equation (2) in order to take into account the drag due to the separation and it can be modelled as in Equation (4).

$$C_D = C_{D_0} + \frac{{C_L}^2}{\pi\, AR} + C_{D_{sep}}, \text{ where } C_{D_{sep}} = k\, \frac{SA_{sep}}{SA}, \text{ and } k = 0.31 \qquad (4)$$

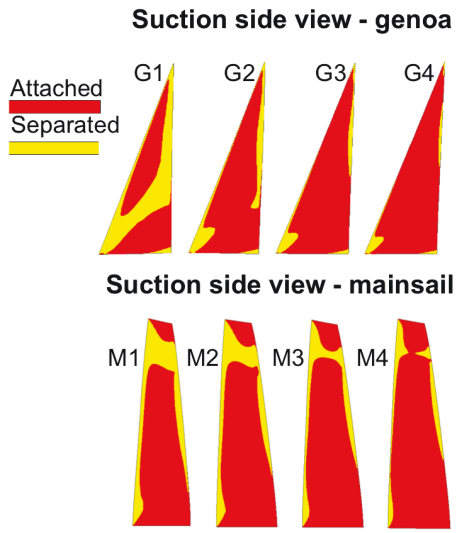

Fig. 16. Attached and separated flow areas on the suction side of the sails: four genoa trims for the mainsail trim M2 and four mainsail trims for the genoa trim G3 (maximum C_x is achieved for M2G3)

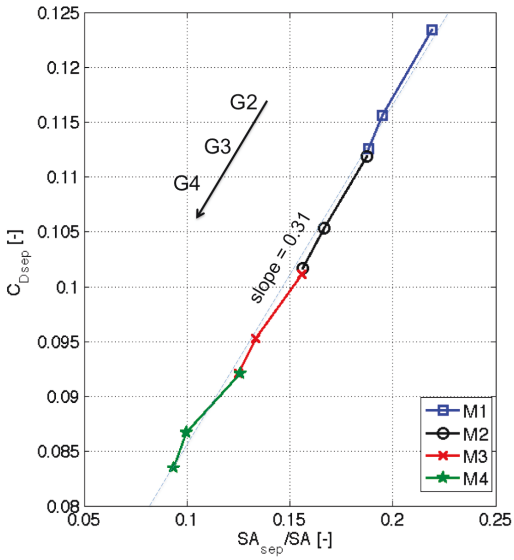

Fig. 17. Additional pressure drag versus the ratio between the sail area with separated flow and the total sail area for three genoa trims (G2-4) and four mainsail trims (M1-4).

This model allows the drag coefficient to be predicted for every trim if the separated sail area is known. Solid lines in Fig. 15 show C_D versus ${C_L}^2$ computed with Equation (4). The force coefficients computed with the CFD simulations and with the proposed theoretical model are in good agreement for all the trims except the tightest genoa trims, where the model over-estimates the drag. This good agreement reveals that it is appropriate to consider an additional drag, proportional to the ratio of separated area on the sails, which may be considered as a pressure drag.

Further investigations should aim at establishing if the adopted values for k can be used with reasonable accuracy for a wide range of sails and conditions. It is interesting to note that this method may allow the aerodynamic forces to be estimated in real sailing conditions, if the separation of the boundary layer can be detected on the sail surface. This is the aim of the tell-tales classically used on sails to help trimming.

5. Conclusions

CFD simulations of fully three-dimensional sails are performed with a RANS approach and validated with local surface pressure measurements obtained with model-scale pressure-tapped rigid sails in an open jet wind tunnel by Viola et al. (2011). The sixteen sail trims measured by these authors were modelled.

In order to model the blockage due to the wind tunnel walls, an original approach is used. In particular, two numerical models of more than one million cells each were developed with structured grids. In the first model, a large area around the open jet section was modelled to accurately determine the onset flow at the open jet section. Boundary layers of the tunnel walls were modelled, while a free-slip condition was used for the sails. The flow field obtained at the tunnel jet test section is used as inlet boundary condition for the second numerical model. The latter model is focussed on the flow around the sails, where a refined mesh enables the sail boundary layers to be accurately modelled.

The analysis of the results of the first model showed that estimating the blockage of the wind tunnel walls leads to a reduction of the lift generated by the sails of more than 1% and an increase of the drag by less than 1%.

The pressure distributions on the sail surfaces computed with the second model were in good agreement with the experimental measurements. In particular, the pressure coefficient was computed with an uncertainty of 0.75% with a confidence level of 95%, allowing the leading edge suction peak and the curvature related suction peak to be well predicted both in amplitude and in their position along the chord. The validation of the simulations with the local pressure measurements allowed, for the first time, a high confidence level in the modelled local flow field near the sails. Therefore, the measured pressure distributions were correlated with the computed flow field. It was found that a laminar separation bubble occurs at the leading edge of the sail and that turbulent reattachment occurs in a strong adverse (positive) pressure gradient. Also, trailing edge separation occurs in a moderate adverse pressure gradient, leading to a gradual levelling of the pressure gradient in the separated region.

The aerodynamic forces are discussed with a particular emphasis on the aerodynamic force projection on the sailing course, namely the drive force. It is highlighted that the optimum sail trim does not correspond to the maximum lift or to the maximum lift to drag ratio, as is known by sail aerodynamicists, particularly in light wind conditions. The distribution of the local drive force can be computed from the pressure distribution and the surface orientation. This gives quantitative confirmation that the fore part of the genoa (fore sail) gives the most part of the drive force and that the effect of the mainsail (aft sail) is mostly to produce an upwash effect on the genoa.

The numerical simulations enable the areas where the flow detaches from the suction side of the sails to be identified. It is shown that when the sails are trimmed to allow the maximum drive force, about 10% of the genoa area and 20% of the mainsail area undergo a separated flow on the suction side. A leading edge separation bubble and a trailing edge separation are highlighted on most of the span of both sails.

In these conditions, the classical potential flow model considering form drag and induced drag is shown to underestimate the drag coefficient evolution with the lift coefficient. In this

paper, an additional pressure drag due to the flow separation is proposed with a linear dependence on the area fraction of separated flow. This new model, with one free parameter to be determined, is shown to fit the results much better than the usual form drag and induced drag only, even if no friction drag is explicitly considered.

Acknowledgements

The authors would like to thank Dr Simon Benson for reviewing this paper and providing suggestions. Also, the third author would like to thank the Yacht and Superyacht Research Group of the School of Marine Science and Technology of the Newcastle University for welcoming him during his stay, as well as the financial support from Brest Métropole Océane and the ERASMUS scholarship kindly awarded by his school, Arts et Métiers ParisTech.

References

Augier, B., Bot, P., Hauville, F., Durand, M., 2012. Experimental validation of unsteady models for fluid structure interaction: Application to yacht sails and rig. J. Wind Eng. Ind. Aerodyn. 101, 53-66.

Campbell, I.M.C., 1997. Optimisation of a sailing rig using wind tunnel data. In: The 13th Chesapeake Sailing Yacht Symposium, Annapolis.

Caponnetto, M., Castelli, A., 1998. America's Cup Yacht Design Using Advanced Numerical Flow Simulations. EPFL Supercomputing Review 10, 24-28.

Chapin, V.G., De Carlan, N., Heppel, P., 2011. A multidisciplinary computational framework for sailing yacht rig design and optimization through viscous FSI. In: The 20th Chesapeake Sailing Yacht Symposium, Annapolis.

Fluck, M., Gerhardt, F.C., Pilate, J., Flay, R.G.J., 2010. A comparison of potential flow based and measured pressure distributions over upwind sails. Journal of Aircraft 47 (6), 2174–2177.

Fossati, F., Muggiasca, S., Viola, I.M., 2006. An Investigation of Aerodynamic Force for IMS Rule Using Wind Tunnel Techniques. In: The 19th HISWA Symposium, Amsterdam.

Gentry, A.E., 1971. The Aerodynamics of Sail Interaction. In: The 3rd AIAA Symposium on the Aero/Hydronautics of Sailing, Redondo Beach.

Gentry, A.E., 1988. The Application of Computational Fluid Dynamics to Sails. In: The Symposium on Hydrodynamic Performance Enhancement for Marine Applications, Newport.

Hedges, K.L., Richards, P.J., Mallison, G.D., 1996. Computer Modelling of Downwind Sails. J. Wind Eng. Ind. Aerodyn. 63, 95–110.

Lasher, W.C., Richards, P.J., 2007. Validation of Reynolds-Averaged Navier-Stokes Simulations for International America's Cup Class Spinnaker Force Coefficients in an Atmospheric Boundary Layer. Journal of Ship Research 51 (1), 22–38.

Marchaj, C.A., 1964. Sailing Theory and Practice. Dodd Mead and Co.

Menter, F.R., 1993. Zonal two-equation k-ω turbulence model for aerodynamic flows. AIAA Paper, 1993-2906

Menter, F. R., Kuntz, M., Langtry, R., 2003. Ten Years of Industrial Experience with the SST Turbulence Model. Turbulence, Heat and Mass Transfer 4, Hanjali´c, K., Nagano Y., Tummers M. (Eds.), 625-632, Begell House.

Milgram, J.H., 1968a. The aerodynamics of sails. In: The 7th Symposium of Naval Hydrodynamics, Rome.

Milgram, J.H., 1968b. The analytical design of yacht sails. In: The SNAME annual meeting, 118–160.

Miyata, H., Lee, Y.W., 1999. Application of CFD simulation to the design of sails. Journal of Marine Science and Technology 4, 163–172.

Renzsh, H., Graf, K., 2010. Fluid structure interaction simulation of spinnakers getting closer to reality. In: International Conference on Innovation in High Performance Sailing Yachts, Lorient, France.

Schlichting, H. T., Gersten, K., 2000. Boundary-Layer Theory. Springer, Berlin.

Shabbir ,A., Zhu, J., 1995. A New k-ε Eddy-Viscosity Model for High Reynolds Number Turbulent Flows - Model Development and Validation. Computers & Fluids 24 (3), 227-238.

Eça, L., Vaz, G., Hoekstra, M., 2010a. Code Verification, Solution Verification and Validation in RANS Solvers. In: ASME 29th Int. Conf. OMAE2010, Shanghai, China.

Viola, I.M., Flay, R.G.J., 2011a. Sail Pressures from full-scale, wind-tunnel and numerical investigations. Ocean Engineering 38, 1733-1743.

Viola, I.M., Flay, R.G.J., 2011b. Sail Aerodynamics: Understanding Pressure Distributions on Upwind Sails. Experimental Thermal and Fluid Science 35 (8), 1497-1504.

Viola, I.M., Flay, R.G.J., 2010. Full-scale Pressure Measurements on a Sparkman & Stephens 24-foot Sailing Yacht. J. Wind Eng. Ind. Aerodyn. 98, 800-807.

Viola, I.M., Pilate, J., Flay, R.G.J., 2011. Upwind Sail Aerodynamics: a Pressure Distribution Database for the Validation of Numerical Codes. International Journal of Small Craft Technology, Trans. RINA 153, (B1), 47-58.

Viola, I.M., 2009. Downwind sail aerodynamics: A CFD investigation with high grid resolution. Ocean Engineering 36, 974-984.

Wilkinson, S., 1984. Partially Separated Flows Around 2D Masts and Sails. Ph.D. Thesis. University of Southampton, UK.